Observing Galaxy Clusters with the AMiBA

Kai-Yang Lin[1,2], Chao-Te Li[1], Paul T.P. Ho[1,3], Chih-Wei Locutus Huang[2], Yu-Wei Liao[2], Guo-Chin Liu[1,4], Patrick M. Koch[1], Sandor M. Molnar[1], Hiroaki Nishioka[1], Keiichi Umetsu[1], Fu-Cheng Wang[2], Jiun-Huei Proty Wu[2], Michael Kestevan[5], Mark Birkinshaw[6], Pablo Altamirano[1], Chia-Hao Chang[1], Shu-Hao Chang[1], Su-Wei Chang[1], Ming-Tang Chen[1], Pierre Martin-Cocher[1], Chih-Chiang Han[1], Yau-De Huang[1], Yuh-Jing Hwang[1], Fabiola Ibañez-Roman[1], Homin Jiang[1], Derek Y. Kubo[1], Peter Oshiro[1], Philippe Raffin[1], Tashun Wei[1], Warwick Wilson[5], Ke-Jung Chen[1], and Tzihong Chiueh[2]

ABSTRACT

The Y.T. Lee Array for Microwave Background Anisotropy (AMiBA) started scientific operation in early 2007. This work describes the optimization of the system performance for the measurements of the Sunyaev-Zel'dovich effect for six massive galaxy clusters at redshifts $0.09 - 0.32$. We achieved a point source sensitivity of 63 mJy per hour of on-source integration with the seven 0.6-m dishes. For a platform mounted interferometer, we measured and compensated for the delays between the antennas. To cancel instrumental instabilities and ground pick up, we employed beam switching where the same local environments are subtracted. Total power and phase stability were good on time scales of hours, and the system was shown to integrate down on equivalent timescales of 300 hours. While the broadband correlator provides good sensitivity, the small number of lags in the correlator resulted in poorly measured bandpass response. We corrected for this by using external calibrators.

Subject headings: CMB — galaxy clusters: general — SZ effect — Instrument: AMiBA

[1]Academia Sinica Institute of Astronomy and Astrophysics, P.O. Box 23-141, Taipei, Taiwan 106

[2]National Taiwan University, Taipei, Taiwan 106

[3]Harvard-Smithsonian Center for Astrophysics, 60 Garden Street, Cambridge, MA 02138, USA

[4]Department of Physics, Tamkang University, 251-37 Tamsui, Taipei County, Taiwan

[5]Australia Telescope National Facility, Epping, NSW Australia 1710

[6]University of Bristol, Tyndall Avenue, Bristol BS8 1TL, UK

1. Introduction

The angular power spectrum of cosmic microwave background (CMB) anisotropies carries a wealth of information on the physical processes in early epochs of the universe. A comparison of theoretical models with accurate measurements of CMB anisotropies thus constrains the fundamental cosmological parameters and models for cosmic structure formation. On larger angular scales, the temperature anisotropies are dominated by primary CMB fluctuations, whereas on smaller angular scales, secondary effects such as the Sunyaev-Zel'dovich (SZ) effects due to galaxy clusters dominate over primordial anisotropies. The amplitude and location of the peak in the thermal SZ power spectrum are particularly sensitive to the amplitude of the primordial matter power spectrum, represented by the normalization σ_8, as well as the thermal history of the hot intracluster medium. The Cosmic Background Imager (CBI, Pearson et al. 2003) and Arcminute Cosmology Bolometer Array Receiver (ACBAR, Kuo et al. 2004) measured the CMB temperature power spectrum at large angular multipoles of $l \sim 3000$, and detected an excess power over the theoretical prediction from the standard cosmological model. However, the uncertainties of the high-l measurements remain large. More accurate measurements on large angular scales around and beyond $l = 3000$ are required to better constrain the value of σ_8 (e.g., Bond et al. 2005; Goldstein et al. 2003; Lin et al. 2004).

The Y.T. Lee Array for Microwave Background Anisotropy (AMiBA, Ho et al. 2008; Chen et al. 2008; Koch et al. 2008a) is designed to measure CMB anisotropies on these multipole scales. The AMiBA is located on the volcanic mountain Mauna Loa, Hawaii, at an altitude of 3400m. The array observes with a single sideband $86 - 102$ GHz, or roughly 3 mm, with cooled HEMT low noise amplifiers (LNA) and correlates using analog lag-correlators. All antennas and receivers are mounted on a 6 m platform to maximize the short spacing sensitivity. In the 2007 and 2008 seasons, observations were done with 60 cm diamter dishes close-packed in the center of the platform. Wu et al. (2008) present details of the observations and analysis of six massive clusters. In this paper we describe how the system performance was optimized for these targeted observations. Two companion papers discuss the data integrity (Nishioka et al. 2008) and the CMB and foreground uncertainty in the SZ flux estimation (Liu et al. 2008). Combined with published X-ray parameters, the SZ fluxes of six clusters were used to measure the Hubble parameter (Koch et al. 2008b) and to examine the scaling relations (Huang et al. 2008). Subaru weak lensing data of four of the clusters were analyzed with the SZ measurements to derive the baryon fraction (Umetsu et al. 2008).

This paper is organized as follows. Critical issues such as the noise temperatures, delay corrections, stability, spurious signal removal and characteristics of the correlators are described in §2. §3 discusses the losses of the system, the calibration errors, and the integration of noise. Finally §4 summarizes our conclusions.

2. OPTIMIZING INTERFEROMETER PERFORMANCE

Prior to and during the 2007 observing season, commissioning activities identified parts of the operations which needed to be improved (Lin et al. 2008). In particular, Huang et al. (2008) reports on the deformation of the platform which can affect the performance of the interferometer. Fortunately, these platform errors are repeatable and can be modeled. Their effects on pointing, radio alignment, and phase errors are discussed in Koch et al. (2008a). For the current operations of AMiBA, these effects were minimal. In this paper, we concentrate on other areas of the interferometer performance which were optimized.

2.1. System Temperature

To understand the gain stability of AMiBA, we first measured the receiver stabilities. The system temperature is monitored by a set of sky-dips in total power mode. The total power output from each IF channel can be approximated by

$$\begin{aligned} P_{IF} &= gkB[T_{rx} + T_{dish} + T_{cmb} \\ &\quad + T_{atm}/\sin(el) + T_{gnd}(az, el)], \end{aligned} \tag{1}$$

where g is the power gain, k is the Boltzmann constant, B is the bandwidth of each IF channel, and the T's denote the noise temperatures from the receiver (rx), antenna ($dish$), CMB (cmb), the atmosphere (atm), and ground pickup (gnd). A hot/cold load measurement is used to calibrate gB and T_{rx}. The receiver noise temperatures are about $55 - 75$ K (Chen et al. 2008). Fitting the total power to $P = P_0 + P_1/\sin(el)$ lumps the contributions into sky-like (P_1) and receiver-like (P_0) parts. The measurements show that the total receiver-like noise temperature is slightly higher than T_{rx} but within measurement errors (~ 5 K). The sky-like part is approximately 15 K at zenith in typical observing conditions. Including T_{cmb}, the system temperatures are about $80 - 100$ K. Under good weather conditions, the system temperatures were quite stable. Hence, we monitored the system temperature in order to reject inferior sky conditions and unstable instrument behavior.

2.2. Delay Correction

Since AMiBA is a coplanar array, there is no fringe rotation in a tracking observation. Fringes occur when a source moves across the field of view (fov) creating a geometric delay. The fov of AMiBA equipped with 0.6-m dishes is $23'$(Wu et al. 2008). The requirement on delay trimming is that the source delay should remain within the sampling range of the lag-correlator, which is ± 50 ps. As the source delay approaches the limit of sampling range, the error in the recovered visibility becomes larger with a consequent rapid drop in sensitivity. To allow a 2-m baseline to observe a $23'$ fov, which corresponds to a delay range of $\sim \pm 22$ ps, the instrumental delay was specified to a tolerance of ± 20 ps.

To measure the delay for each correlation, all dishes were removed and a noise source was mounted between receivers (e.g. Ant_1 and Ant_2). A fringe is generated when the noise source moves from Ant_1 toward Ant_2, simulating a fringe due to a celestial source.

$$L(x, \tau_a) = \mathcal{R}\left(\int_{IF} df \mathbb{R}'(f) e^{-i2\pi[(f+f_{LO})\frac{2x}{c}+f(\tau_2-\tau_1+\tau_a)]}\right), \tag{2}$$

where x is the displacement of noise source, f is the IF frequency, and $\mathbb{R}'$ is the complex response function of the baseline excluding the linear part of the phase due to lags (τ_a, $a = 1...4$) in the correlator. $\mathcal{R}$ takes the real part of the expression and is done implicitly whenever necessary hereafter. τ_1 and τ_2 represent the instrumental delay in the IF's of Ant_1 and Ant_2. The fringe envelope peaks when $\frac{2x}{c} = \tau_1 - \tau_2 - \tau_a$. The relative delay $\tau_1 - \tau_2$ is measured with respect to the central lag (with $\tau_a = 0$). Equation (2) is usually referred to as the lag output or the lag data throughout this work.

We found the instrumental delays for all IF channels using relative delay measurements. Short cables were then inserted into each IF for compensation. After this trimming procedure the residual delays were measured by fitting fringes for the Sun without the dishes, modeling the fringes as the convolution of the observed point source fringe with a circular disk. The differences between observation and model are consistent with residual delays of ± 15 ps (RMS). Except for the delays due to platform deformation, the delays between antennas were therefore well controlled.

2.3. Bandpass Shape Measurement

AMiBA correlator has four lags and outputs two spectral channels to cover the 16GHz bandwidth. Knowing the bandpass shape is an important aspect of obtaining good visibility using this type of correlator (see next section §2.4). Because the analog correlator contributes significantly to the bandpass shape, we took the baseline-based measurement approach. The

Fourier transform of the fringe $L(x, \tau_a)$ against x is used to determine $\mathbb{R}'$ for each baseline, with a spectral sampling of about 0.8 GHz. Fig. 1 displays the gain and phase responses of all valid measurements after four lag outputs of each correlator are averaged together.

The conversion from observed fringe rate to the RF frequency is proportional to the noise source translation speed. We believe a ± 1 % jitter is present in the translation stage we used, which introduced roughly ± 1 GHz uncertainty in the response frequency. This effect is one of the major problem when trying to apply a more accurate visibility extracting method to our data. The discussion is in the next section. Improved measurement setup involving simultaneous injection of a single frequency source is being experimented to achieve a higher accuracy.

The effective bandwidths, defined as $B = |\int df \mathbb{R}'|^2 / \int df |\mathbb{R}'|^2$, are insensitive to the translational error of frequency. Based on our bandpass measurements, the effective bandwidths of AMiBA are calculated and shown in Fig.2. They generally fall in the range of $7 - 13$ GHz.

2.4. Extracting the Interferometer Visibilities

Several approaches can be used to convert the four measured lags of the AMiBA correlator into complex visibilities in two channels over the 16 GHz bandwidth. We find that the inaccuracies inherent in this inversion need to be corrected by external calibration. Here we adopt the formalism of Wu et al. (2008) (see Li et al. 2004, for an alternative formalism). The lag output in equation (2) can be expressed in matrix form as $L_a = \mathbb{R}_{ak} \mathbb{V}_k^{src}$, where $\mathbb{V}_k^{src}$ is the source visibility. Subscript a indexes the $N_{lag} = 4$ lags, and subscript k indexes the N_f discretized frequency samples f_k, where N_k is usually much larger than N_{lag}.

The transformation relies on a kernel $\mathbb{K}_{ak}$, which is an estimate of the response matrix $\mathbb{R}_{ak}$. The kernel is integrated in frequency into two channels $\overline{\mathbb{K}}_{ac}$, where $c = 1...4$ indexes the real and imaginary parts of the two channels. We use the inverse of the integrated kernel to construct the raw visibility $\mathbb{V}_c^{raw} \equiv \overline{\mathbb{K}}^{-1}{}_{ca} L_a$.

It turns out that $\mathbb{K}_{ak}$ is an inaccurate representation of $\mathbb{R}_{ak}$, due to measurement errors, variations with temperature or time, insufficient spectral resolution in the measurement, or insufficient information about the response. Fig. 3 demonstrates the calculation of raw visibility using simulated drift scans in three cases when (1) the kernel is the exact response, (2) there are measurement errors, and (3) there is no knowledge about the response. The correct visibility should appear as a Gaussian in amplitude with a linearly increasing phase. Deviations from this form increase with decreasing accuracy of the kernel. We therefore must

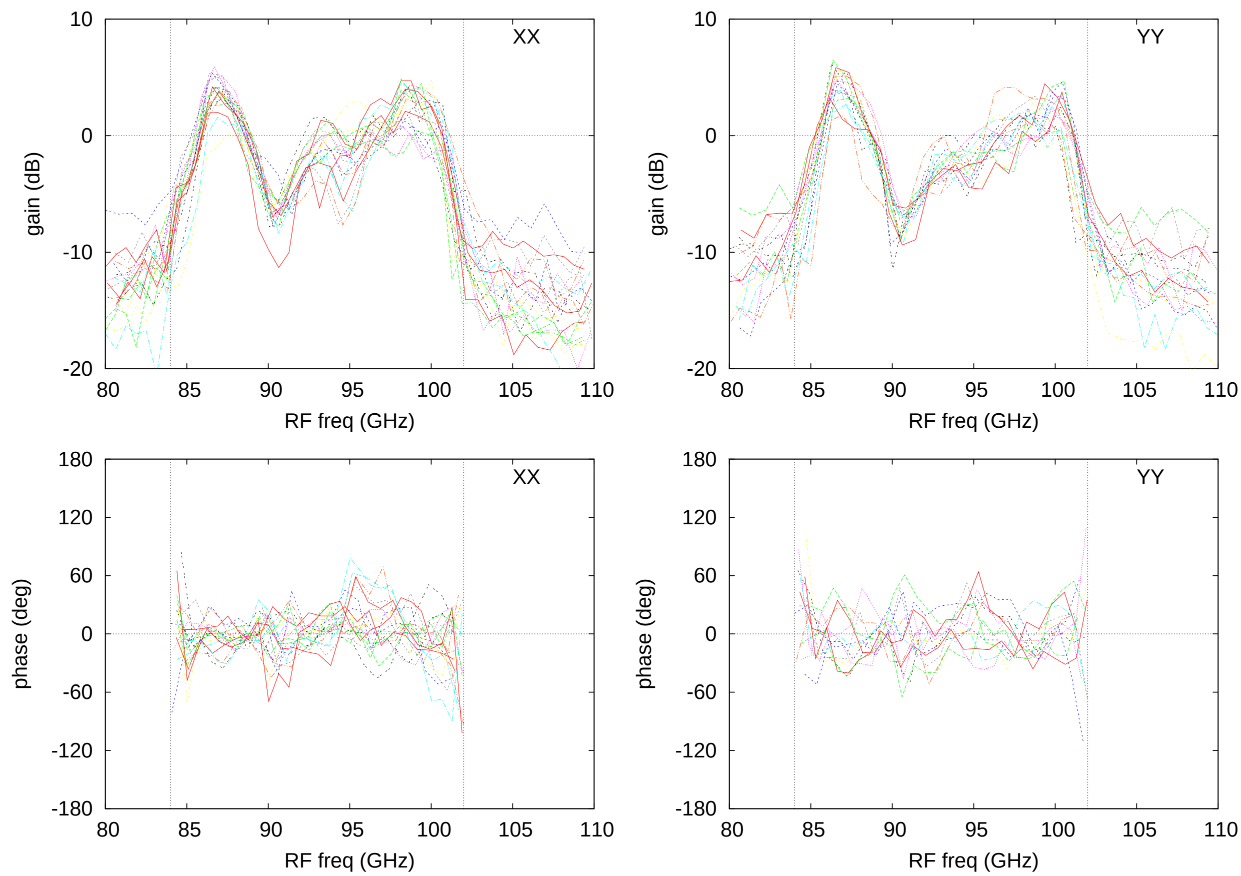

Fig. 1.— The complex responses of AMiBA. Responses include effects from the RF components, IF components, and the analog correlator. Top and bottom pannels display the gain and phase responses respectively, while the responses for XX correlations and RR correlations are separated in the left and right pnaels. Each line represents a receiver pair and correlator combination.

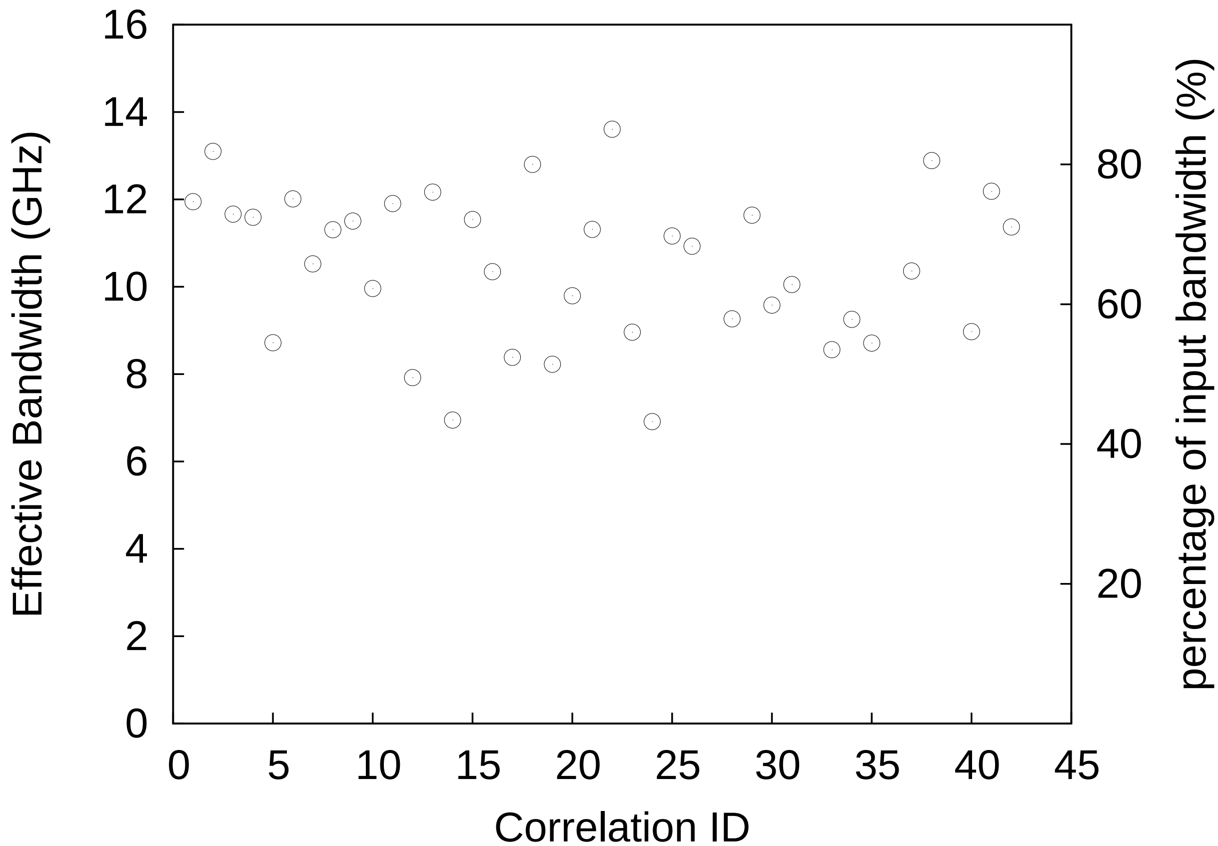

Fig. 2.— Effective bandwidths of the AMiBA correlators calculated from the bandpass displayed in Fig.1. The percentage is based on the nominal input bandwidth of 16 GHz.

obtain a calibrated visibility from the raw visibility $\mathbb{V}_b^{cal} \equiv C_{bc}\mathbb{V}_c^{raw}$, where b has the same index range as c, and C_{bc} is the calibration matrix, which can be obtained by comparing the raw visibility of a planet (the calibrator) to the theoretical visibility.

In the analysis of data taken in 2007, the flat kernel (right-most function in Fig. 3) was assumed, and planet calibrations were applied. We have estimated the errors introduced by external calibration by running simulations on point source models. This error is on the order of $\pm 2\%$ (1σ) in the absolute fluxes. This is small compared to the thermal noise and the measurement errors on the planet itself.

2.5. Stability

The stability of the system was examined by measuring the variation in visibilities for a few bright planets during local times 8 pm to 8 am, as normally used for observing. For this test, ephemeris of the planets were taken at the beginning of each track but not updated since, which results in a pointing error that increases by about an arcminute over 12 hours. To account for this, two sets of visibility data for each planet were chosen as calibrating events. A linear interpolation was used to remove the linear drift. For data without bracketing events, the nearest calibration was used. Fig. 4 demonstrates an example of the stability measurement result. The gain stability was found to have an RMS variation around 5%, and the phase to have an RMS variation around 0.1 rad. The measurements also reveal that phase response is more sensitive to changes in environment than gain response, especially in the first hour after shelter opening.

Fig.5 plots the flux of Jupiter recovered from the same data set as in Fig.4. Data was calibrated by the first measurement at UT 12h (not plotted). The recovered flux varied within $\pm 4\%$ of the expected flux till sunrise. Calculation of calibrator flux is discussed in §3.2.

Based on the stability measurements, we chose to use a calibration interval of two to three hours, to give calibrations good to about 5% in gain and 0.1 rad in phase for each baseline. Calibration requires $\sim 10\%$ of telescope observing time.

2.6. Minimizing Instrumental and Ground Pickup

When AMiBA tracks a source the signal in the lag output should be constant in time. However, the weak signal we measure is susceptible to slowly-varing contamination. The system was designed with a phase switching and demodulation scheme to remove contami-

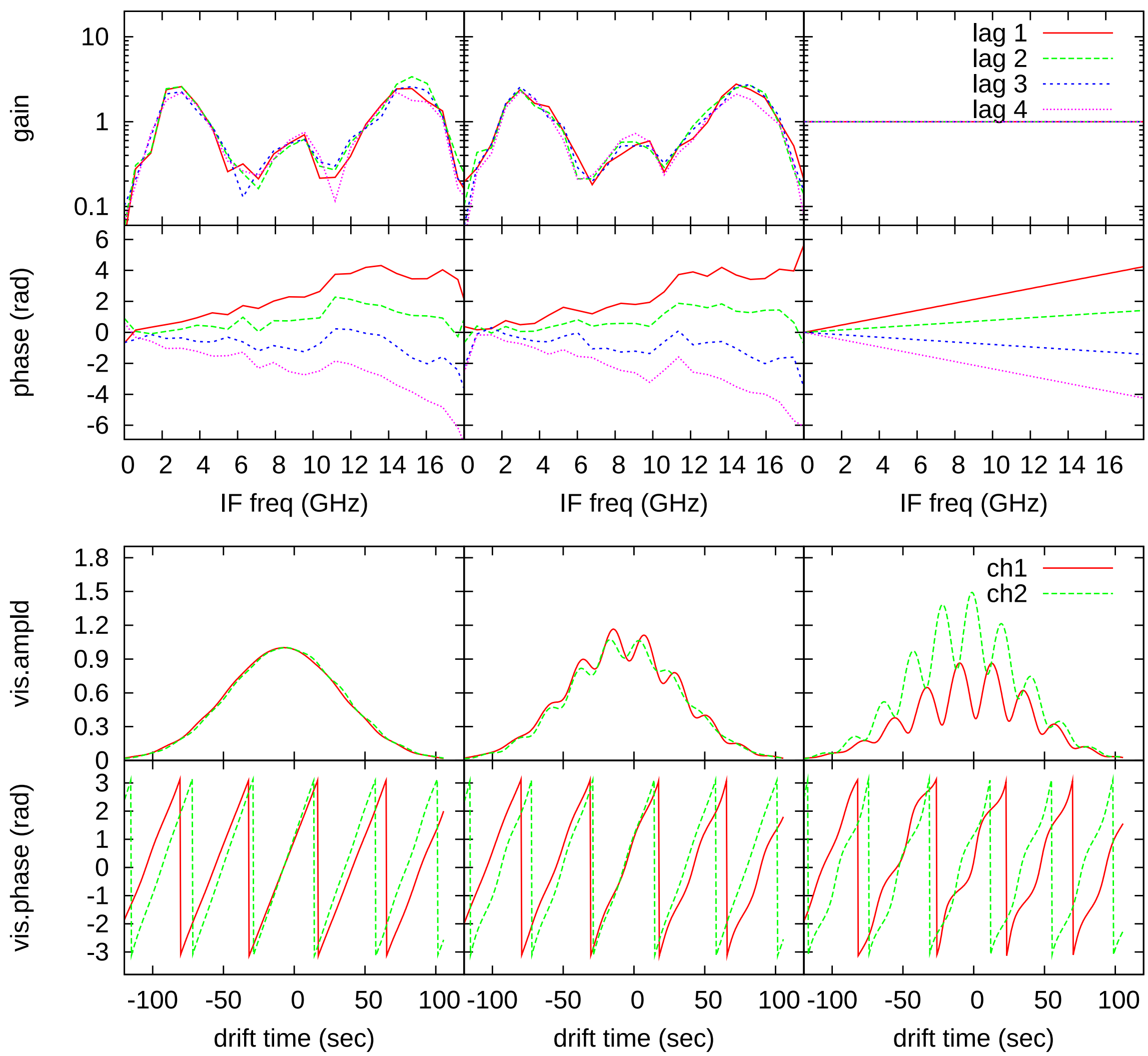

Fig. 3.— The upper panel shows the complex lag-to-visibility kernels. A simulated drift scan was generated using the left-most function and a flat source spectrum. The lower panel shows the raw visibilities from kernels in corresponding columns. The horizontal axis is the source offset presented as drift time. To the left we see the case when the kernel is the same as the response function. The central plots show the results with small errors in the kernel. On the right we show the result of using an ideal flat kernel. A proper calibration removes the visibility error and produce good imaging results (see §2.4).

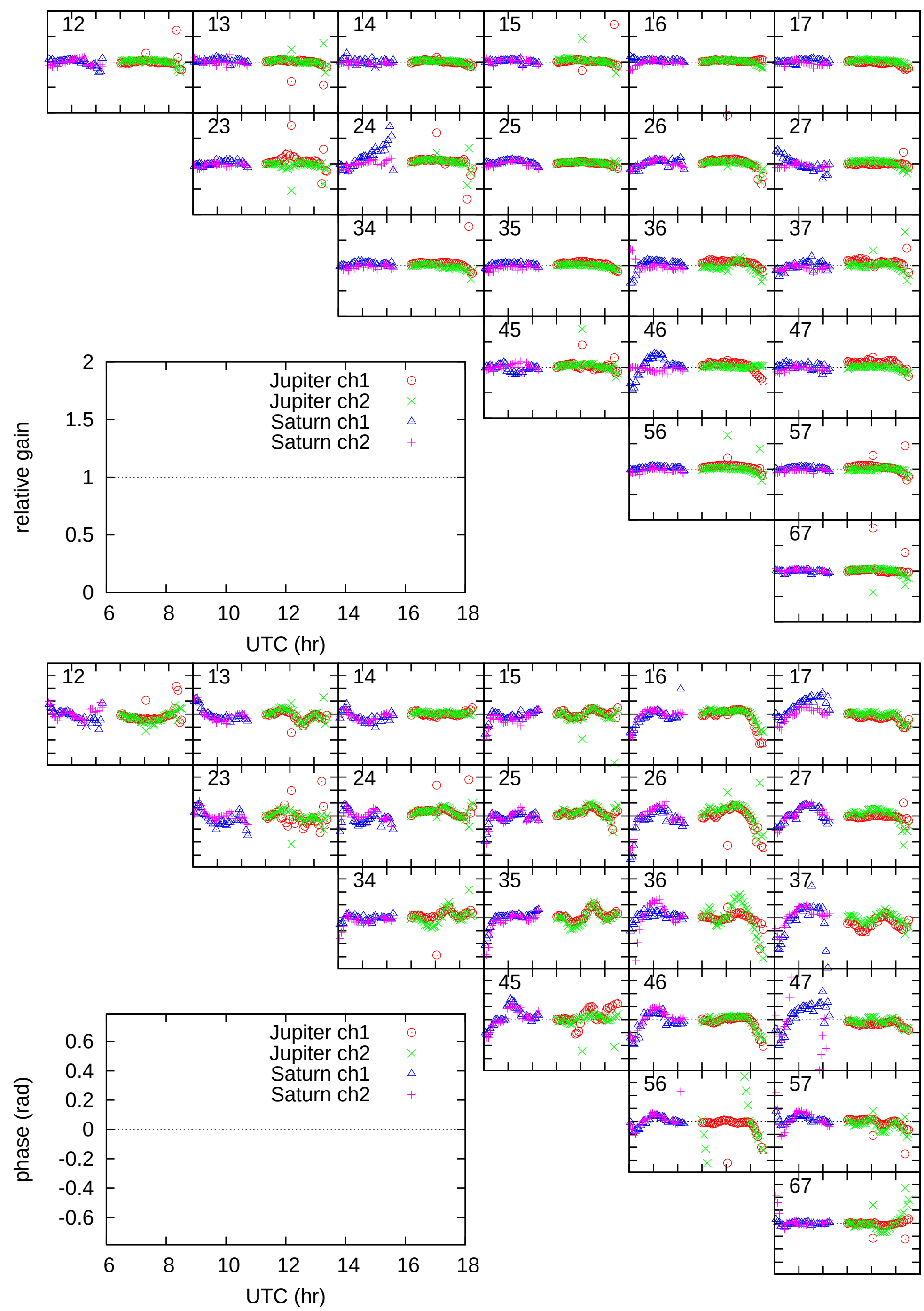

Fig. 4.— Visibilities recovered from a repeated two-patch tracking of Saturn (open triangles and plus symbols) and Jupiter (open circles and cross symbols) in the local time range 8 pm to 8 am (UT 6hr to 18hr). The upper panel shows the relative gain fluctuation, and the lower panel shows the phase variation of the XX correlations. The scale of the plot as well as the time range are indicated at the bottom left subplot of each panel.

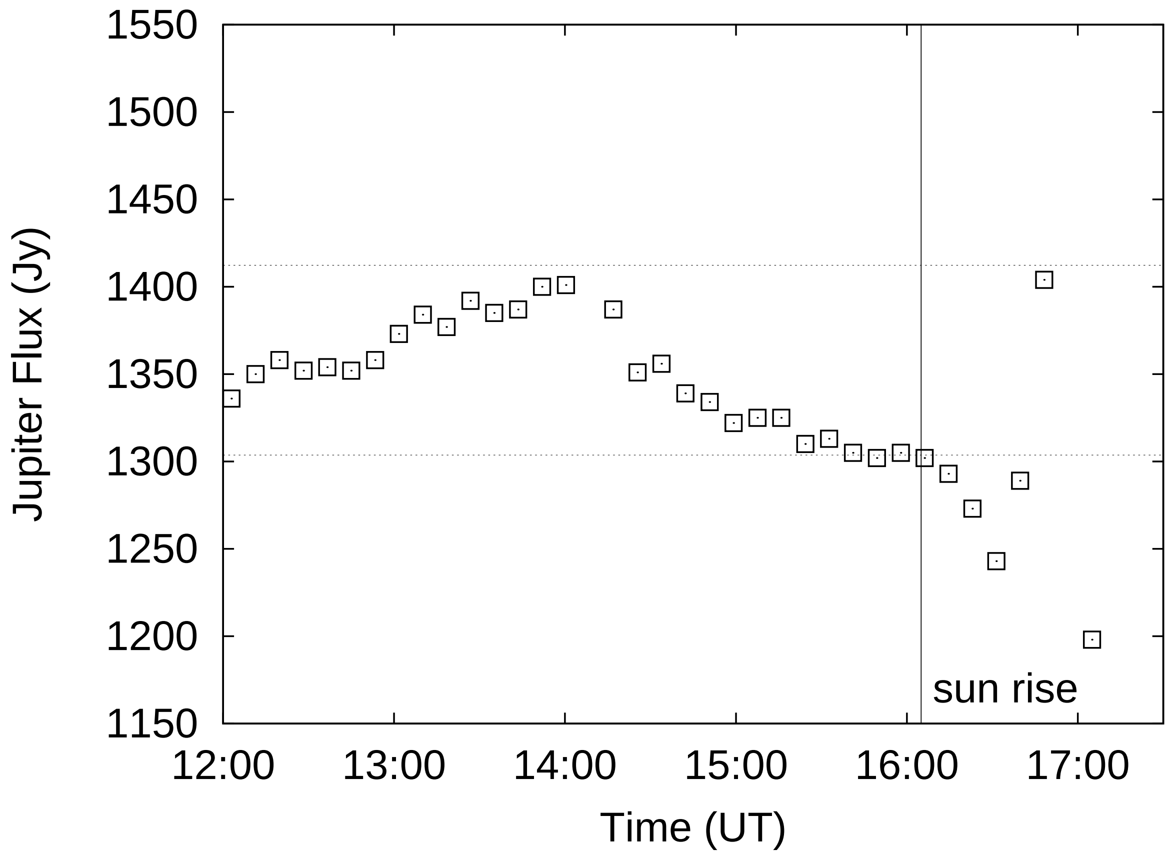

Fig. 5.— Jupiter flux recovered from the stability measurements as shown for each baseline in Fig.4. Two horizontal dotted lines indicate ±4% of the expected Jupiter flux.

nation between the mixer and the correlator readout. However, the mixers in the correlator can pick up higher-order signals such as $|E_1|^2|E_2|^2$ in addition to their nominal output which is proportional to $E_1E_2^*$ or $|E|^2$, where E_i stands for the voltage from Ant_i. If the power of the IF signal is modulated by the phase switching pattern, then this higher order response can generate an output that is coherent with the demodulation pattern and becomes a spurious signal. This issue indeed exists in AMiBA, where phase switching of the LO is done by changing between two signal paths that can differ by 0.3 dB in total power. The LO power modulation is carried through to the IF in varying amounts depending on the mean LO power level at the mixer. The IF modulation can be undetectable for optimally-tuned mixers, but is up to 3 dB for under-pumped mixers.

To reduce the IF modulation, the LO drive level is optimized for minimum conversion loss for each mixer. Modulation of the LO power would then have the least impact on the IF power. Furthermore, to reduce the drifting of LO level with ambient temperature changes, the final amplifier and frequency doubler in the LO chain are operated in the soft saturation regime. Additional protection will be provided by temperature controls installed before the 2008 observing season.

Spurious signals external to the system, such as ground pickup, will still affect the data. We used a subtraction scheme similar to the one used by CBI (Padin et al. 2002) to suppress the slowly-varying signals. In practice, we have found that the spurious signal in individual patches in $\sim$5 hrs integration can be as high as $\pm$7 Jy/beam, but that after subtraction a cluster with brightness 0.3 Jy can be detected at 9σ level in 11 hours (i.e., with 5.5 hours on-source integration). The observing strategy and the data analysis are given in Wu et al. (2008).

3. ACHIEVED SYSTEM PERFORMANCE

3.1. Overall Efficiency

For each baseline, losses include the antenna loss, antenna misalignment, and the correlation loss. The antenna loss is mainly from the optics (illumination efficiency, secondary blockage, and forward spillover), and the overall antenna efficiency is calculatd to be 0.58 in Koch et al. (2008c). The antenna misalignment consists of the mechanical installation error and the dynamical deformation of the platform. The former error was measured to be around $3'$ during the 2007 observing season (Wu et al. 2008, *in preparation*) and will be improved for future observations. The latter error was inferred from photogrammetry measurements of the platform surface to be less than $1'$(Koch et al. 2008a). The two errors together attenuate the primary beam by 2%. Antenna misalignment may also cause pointing errors for some baselines. This effect is not considered in individual baseline efficiencies but will be considered in the array efficiency. There is also a correlation loss from the noise contributed by the rejected correlations in the analog correlator. The estimated efficiency from this cause is 0.81.

When combining baselines from the entire array, pointing error and system stability also lower the efficiency by degrading the coherence of signal from different measurements. The pointing error is less than $0.4'$ (Koch et al. 2008a) and decreases the efficiency by less than 2%. The large alignment error, on the other hand, contributes as much as 12% loss in the 2007 observations. As described in §2.5, the system stability is approximately $\pm 5\%$ in gain and ± 0.1 rad in phase. Combining all baselines results in a reduction of signal by about 2%. Table 1 summarizes the major losses in the system.

The baseline efficiency has been checked by comparing the signal-to-noise ratio (SNR) of Jupiter's fringe to the ratio of Jupiter's antenna temperature and the system temperature. $\eta_{bl} = \mathrm{SNR}_{Jup} / (\frac{T_{a,Jup}}{T_{sys}} \sqrt{B_{eff} \frac{t_{rec}}{2}})$, where $T_{a,Jup}$ is the antenna temperature of Jupiter, typically around 0.1K for the 60cm dishes, and SNR_{Jup} is the SNR of Jupiter under the corresponding recording time t_{rec} ($= 0.452$ sec currently). An average effective bandwidth of $B_{eff} \sim 10$ GHz was assumed in the calculation. The measured efficiency scatters from 0.2 to 0.5 with an error bar of approximately 0.2. The error originates mainly from the noise estimation of the signal-dominant fringe, the occasional large readout noise, and also the variation of effective bandwidth. The overall array efficiency will be covered in §3.3.

3.2. Calibrator

The raw visibilities recovered from the lag data have the systematic losses discussed above and are further affected by instrumental delay, gain drift, phase variation as well as the imperfect lag-to-visibility transformation. We calibrate visibilities by interspersed two-patch observations of a planet. This converts our visibility amplitudes to flux density units and references the phase to the calibrating planet position.

Taking planet data with the subtraction scheme, and applying the same calibration scheme used for cluster data (one calibration about every three hours), we find that the recovered peak flux in the image domain shows an RMS scatter of about 3%.

The flux densities of the planets are calculated from published disk brightness temperatures and the apparent angular sizes assuming a black-body spectrum. We adopt the values: Jupiter 171.8±1.7 K (Page et al. 2003; Griffin et al. 1986), Saturn 149.3±4.1 K

(Ulich 1981), and Mars 206.8±5.6 K (Ulich 1981). Fig.6 shows the recovered flux of the main calibrators (Jupiter and Saturn) in the 2007 and 2008 observations and the expected flux from calculation. For the phase reference and flux standard we use the last Jupiter measurement for each night when Jupiter is observed, and it provides the best calibration for the later arisen Saturn measurements. Scatter of the Jupiter flux agrees with the scatter in one night as shown in Fig.5. Flux of Saturn is systematically lower than the calculated value by approximately 5%. It is verified that the lower flux was not the result of an error in flux standard. It was checked by artificially setting the phase error to zero in the calibrated visibilities of Saturn and forming an image. The recovered flux displays no systematic offset from the calculated level within the error bar. Note that the effect of Saturn's ring is not included in the calculation of Saturn's flux. We estimate that our flux density scale is good to about ±5% in absolute terms.

3.3. Noise Integration

Based on the signal-to-noise ratio (SNR) of Jupiter's fringe and the discussion in §3.1, we find that the array has an overall efficiency of about 0.4. Whether the sensitivity can be applied to longer integration depends critically on the removal of spurious signals using the subtraction scheme and subsequent data flagging. To verify the sensitivity, we examine the variation of signal and noise in the reconstructed map with integration time in Figure 7. The integration time here refers to the accumulation of observing time spent in each individual visibility channel. For example, when the telescope tracks a source for 3 minutes, the total integration time for 21 baselines, 2 polarizations, and 2 channels is $t_{tot} = 180$ sec $\times 21 \times 2 \times 2 =$ 15120 sec. Since the visibilities are used with non-uniform weights in forming the image, we calculate an effective integration time, which for 3 minutes on-source integration is defined as $t_{eff} = \frac{(\sum_i w_i)^2}{\sum_i {w_i}^2} \times 180$ sec, where w_i denotes the weighting given to each data set. In this analysis, a natural weighting is adopted.

Since the noise comes from two patches and the signal comes from only one, the point source sensitivity can be estimated by $\sigma = \frac{2kT_{sys}}{\eta_{all} A_{phys}} \frac{1}{\sqrt{t_{eff} B_{ch}}}$, where $T_{sys} = 100$ K, $B_{ch} =$ 5 GHz, η_{all} is the overall efficiency, and A_{phys} is the physical collecting area.

The signals are read from the source position in the reconstructed dirty images with different integration time. The source position is determined by the final image. A CLEAN (Hogbom 1974) procedure is applied to the inner 21.6′ box, which roughly corresponds to the FWHM of the primary beam. The cleaned signal at the source position is also recorded, while the residual noise is measured in the 1 deg image excluding the inner clean region.

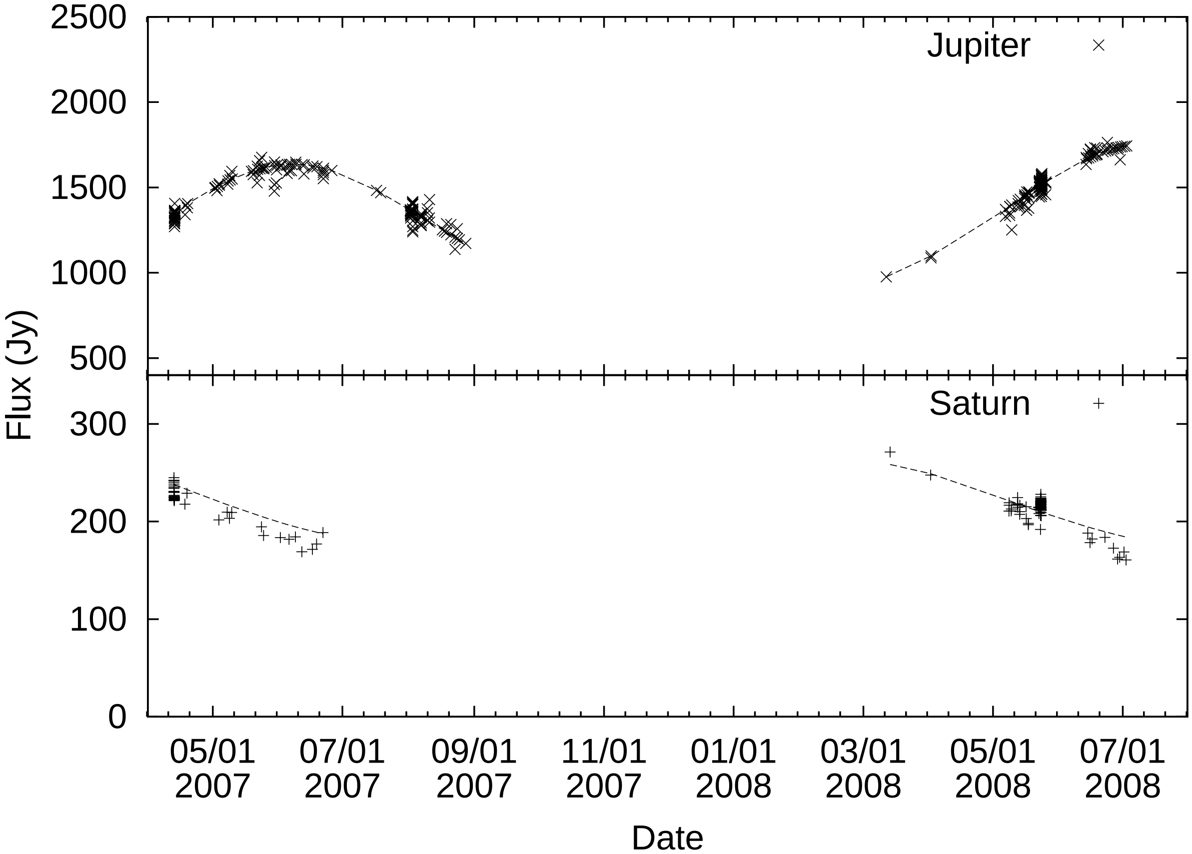

Fig. 6.— The recovered flux of our main calibrators, Jupiter (plus symbols) and Saturn (cross symbols) from the observations in 2007 and 2008. Data were calibrated by the first Jupiter measurement in the same night, or the nearest Jupiter measurement. The expected flux were plotted as dashed and solid lines for Jupiter and Saturn respectively.

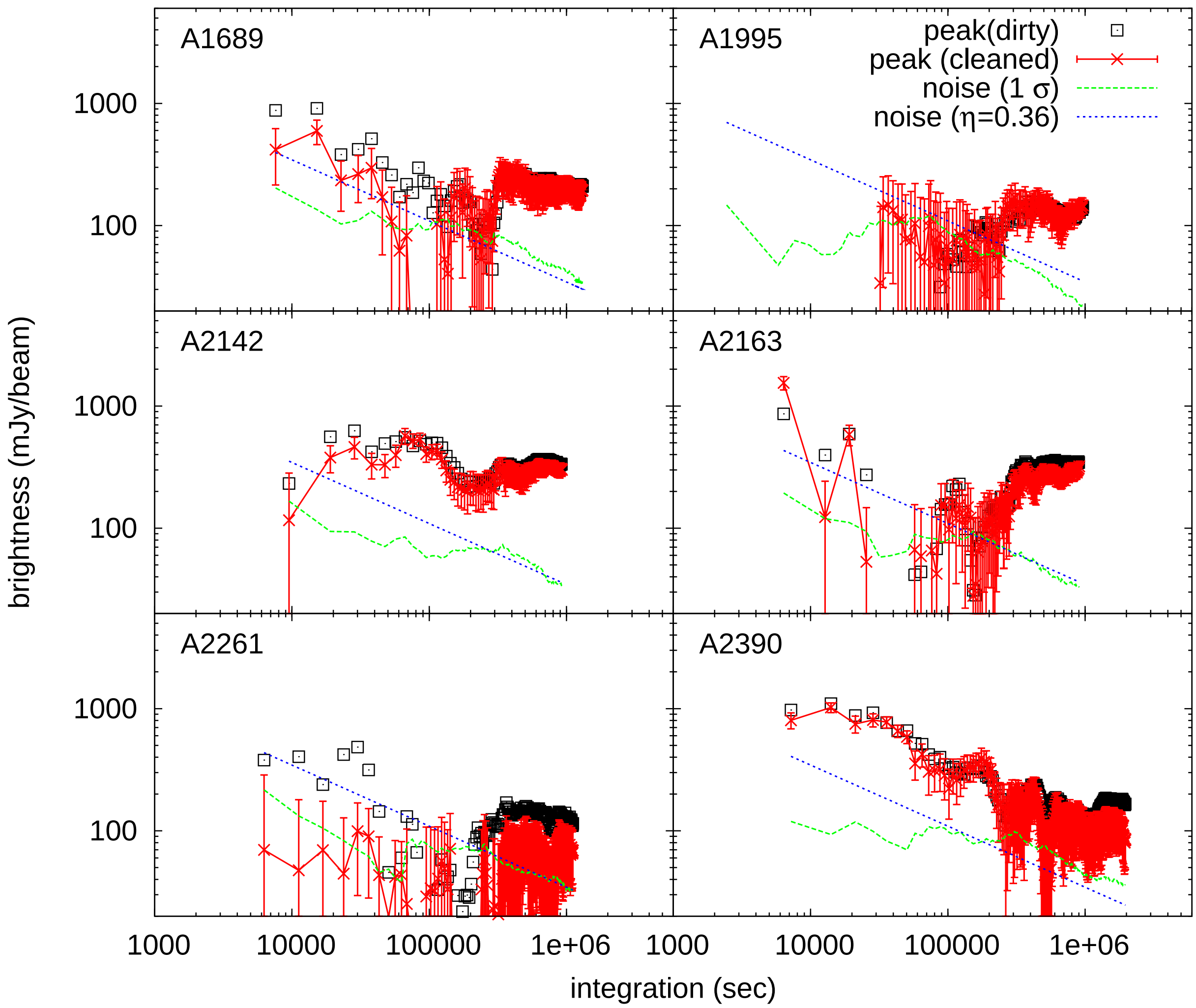

Fig. 7.— The signal and noise plotted against effective integration time for our sample. The black open squares and the red solid line with error bars represent the signal measured in dirty and cleaned maps respectively and have been multiplied by -1 in the plot. The green dashed line shows a noise estimate from the cleaned maps (see §3.3). Finally the blue dotted line shows the expected noise level given the effective integration time, an overall system efficiency of 0.36, and a system temperature of 90 K.

Figure 7 shows that an efficiency $\eta = (0.36 \pm 0.04)$ is more representative for the current data, giving a point source sensitivity of (63 ± 7) mJy per hour of on-source integration. Abell 2390 has a higher noise, and we believe this may be caused by the presence of point sources in the fov. Liu et al. (2008) investigate the contamination by point sources and the primary CMB.

4. Conclusion

To detect galaxy clusters with the AMiBA, we must achieve system stability on timescales of hours. We have optimized the performance of AMiBA by measuring and compensating for the delays between antennas, and using beam switching techniques to cancel out instrumental and environmental effects. Planet calibrations provided corrections for passband response. Overall efficiency for AMiBA was $\eta_{all} = 0.36 \pm 0.04$, with a major loss from the antenna efficiency $\eta_{ant} = 0.58$.

Using a system temperature of 90 K, an effective bandwidth of 5 GHz per channel, and an overall efficiency of 0.36 ± 0.04, the point source sensitivity of AMiBA per hour of on-source integration ($t_{eff} = 302400$ sec) is about 63 ± 7 mJy when the subtraction scheme is applied. The effective integration is about 60% of the on-source integration time. The loss of 40% of observing time is mostly due to lower weighting applied to some receivers or baselines experiencing hardware problems. There were very few observations made when the weather was not good in the 2007 observing season.

The flux error consists of the calibrator flux scale uncertainty of ± 5 %, and the cross-calibration error ± 3%, which also includes the lag-to-visibility flux error of ± 2%. Both are well below the thermal noise in all clusters observed during 2007. Investigation of noise in cleaned images shows that longer integration, aimed at measuring primordial CMB fluctuation, will be promising.

The resulting successful detections of the clusters have led to a number of scientific results including a measurement of the Hubble constant and the study of the hot gas distribution in the clusters. These are discussed further in the companion papers.

Acknowledgments Capital and operational funding for AMiBA came from the MoE and the NSC as part of the Cosmology and Particle Astrophysics (CosPA) initiative. Additional funding also came in the form of an Academia Sinica Key Project. Support from the STFC for MB is also acknowledged.

REFERENCES

Bond, J. R. et al. 2005, ApJ, 626, 12

Chen, M.-T. et al. 2008, ApJ, submitted

Goldstein, J. H. et al. 2003, ApJ, 599, 773

Griffin, M. J. et al. 1986, Icarus, 65, 244

Ho, P. T. P et al. 2008, ApJ, ApJ, submitted (astro-ph/0810.1871)

Hogbom, J. A. 1974, A&AS, 15, 417

Huang, C.-W. L. 2008, ApJ, submitted

Huang, Y.-D. et al. 2008, SPIE, 7012, 70122H

Koch, P. M. et al. 2008a, ApJ, submitted (this issue)

Koch, P. M. et al. 2008b, ApJ, submitted (this issue)

Koch, P. M. et al. 2008c, *in preparation*

Kuo, C.-L. et al. 2004, ApJ, 600, 32

Li, C.-T. et al. 2004, SPIE, 5498, 455

Lin, K.-Y., Woo, Tak-Pong, Tseng, Yao-Huan, Lin, Lihwai, and Chiueh, Tzihong 2004, ApJ, 608, 1L

Lin, K.-Y. et al. 2008, SPIE, 7012, 701207

Liu, G.-C. et al. 2008, ApJ, submitted

Nishioka, H. et al. 2008, ApJ accepted (astro-ph/0811.1675)

Padin, S. et al. 2002, PASP, 114, 83

Page, L. et al. 2003, ApJS, 148, 39

Pearson, T. J. et al. 2003, ApJ, 591, 556

Umetsu, K. et al. 2008, ApJ, submitted (astro-ph/0810.0969)

Wu, J.-H. P. et al. 2008, ApJ, submitted (astro-ph/0810.1015)

Ulich, B. L. 1981, AJ, 86, 1619

Table 1. Summary of Losses of The System

Systematics	Efficiency
Antenna illumination	0.90
Antenna blockage	0.92
Antenna spillover	0.78
Antenna others effects	0.90
Antenna total	$0.90 \times 0.92 \times 0.78 \times 0.90 = 0.58$
Alignment	0.98
Correlation	0.81
Overall Baseline	$0.58 \times 0.98 \times 0.81 = 0.46$
Deformation/Pointing	0.88
Stability	0.98
Overall Array	$0.46 \times 0.88 \times 0.98 = 0.40$